Applied Catalysis B: Environmental 174–175 (2015) 96–104

Contents lists available at ScienceDirect

Applied Catalysis B: Environmental

journal homepage: www.elsevier.com/locate/apcatb

Key role of terminal hydroxyl groups and visible light in the reactive adsorption/catalytic conversion of mustard gas surrogate on zinc (hydr)oxides

Dimitrios A. Giannakoudakis, Javier A. Arcibar-Orozco, Teresa J. Bandosz *

Department of Chemistry and the Graduate School of CUNY, The City College of New York, 160 Convent Ave, New York, NY 10031, USA

ARTICLE INFO

Article history:
Received 27 November 2014
Received in revised form 19 February 2015
Accepted 20 February 2015
Available online 21 February 2015

Keywords:
Zinc hydroxide
Zinc oxide
2-Chloroethyl ethyl sulfide
Reactive adsorption
Photocatalysis

ABSTRACT

Rhombic $Zn(OH)_2$ and flower-like ZnO nano-particles were synthesized with a controlled precipitation rate. The materials were characterized by XRD, FTIR, potentiometric titration, nitrogen adsorption, TA-MS, MS-MS, SEM and UV–vis–NIR. A commercial ZnO was used as a reference material. Hydroxyl groups were formed on the surface when a slow addition of NaOH was used. The surface area of $Zn(OH)_2$ was higher (350%) in comparison to that of ZnO. The presence of hydroxyl groups increased the band gap from 3.05 eV for ZnO to 3.22 eV for $Zn(OH)_2$. The materials were used as reactive adsorbents of mustard gas surrogate, 2-Chloroethyl ethyl sulfide (CEES). On the surface of $Zn(OH)_2$, more CEES was absorbed than of that of ZnO. Moreover, the capacity on $Zn(OH)_2$ significantly increased under a visible light exposure. The results indicated the paramount role of terminal —OH groups in the reactive adsorption process. The porosity was also found important since it affects the distribution of these OH active centers. Ethyl vinyl sulfide (EVS) was detected on the surfaces of both samples. At light, hydroxyethyl ethyl sulfide (HEES) was detected only on $Zn(OH)_2$. Thus the absorption of photons led to the formation of the ethyl ethyl sulfide (EES) cations, which were transformed to less toxic EVS by dehydrohalogenation. With water and hydroxyl groups on the surface, the light irradiation promoted the formation of hydroxyl radicals. They reacted with the EES radicals and formed HEES via a hydrolysis pathway. No conversion of CEES was found in the dark.

1. Introduction

Zinc (hydr)oxides are important materials for catalysis and photocatalysis fields. The size, shape, structure and morphology of zinc oxide/hydroxide crystals formed from aqueous solutions can vary considerably [1]. One of the quickest, economically feasible and green syntheses of zinc oxide/hydroxide is the addition of sodium hydroxide to a zinc salt solution. When NaOH is added to a Zn salt precursor solution, factors such as addition rate, final pH of a solution, and aging time have an effect on the crystal phase and structure [2–4]. Thus, the precipitation/formation of ZnO or $Zn(OH)_2$ can be promoted by controlling the addition rate of the NaOH precipitant. It was found that the properties of precipitates formed from $ZnCl_2$ and a base depend on the pH of the solution and mixing time a slow addition of NaOH led to the formation of ϵ-$Zn(OH)_2$ [4,5], whereas a rapid addition yielded ZnO [6]. Nicholas et al. reported that at temperatures less than 70 °C and using a NH_4OH solution (0.03 M) as a precipitating agent, a würtzite growth from wülfingite was observed after a period of time. The latter was the initially formed stable crystalline compound in the precipitation reaction. Furthermore, by tracking the oxygen atoms via isotope labeling, they determined that the transformation occurs primarily via a solid state to a solid state path [2]. Yamabi and Imai [7] found that wülfingite $Zn(OH)_2$ was predominantly formed at pH 6.0–9.0, while würtzite ZnO was mainly obtained at pH 9.0–13.0 from the reaction of zinc sulfate heptahydrate ($ZnSO_4\,7H_2O$) with ammonium fluoride (NH_4F), ammonium chloride (NH_4Cl), ammonium nitrate (NH_4NO_3), and ammonium sulfate ($(NH_4)_2SO_4$) as complexing agents.

Whereas the adsorptive performance, as well as the photocatalytic properties of the zinc oxide are well known [8,9], the hydrated oxides have attracted less attention, even though they have been reported as superior to oxide in certain applications [10]. The latter is owing to the high reactivity of their OH groups, especially terminal ones, with specific adsorbates. For example, Mabayoje and co-workers [11] found that the efficiency of SO_2 [12], NO_2 [13],

* Corresponding author. Tel.: +1 212 650 6017; fax: +1 212 650 6107.
E-mail address: tbandosz@ccny.cuny.edu (T.J. Bandosz).

http://dx.doi.org/10.1016/j.apcatb.2015.02.028
0926-3373/

and H_2S [10] removal increased with an increase in the number of terminal hydroxyl groups detected on the surface. In addition, those OH groups can represent an important source of active radicals for photoactive reactions [10]. The surface chemical properties of $Zn(OH)_2$ also differ from those of ZnO, and a developed surface area and pore volume might promote the reactive uptake of specific target molecules.

2-Chloroethyl ethyl sulfide (CEES) is a surrogate of bis(chloroethyl) sulfide, also known as mustard gas (HD). The latter is a powerful nerve agent that has been used in the past as a chemical weapon [14]. To the best of our knowledge, the detoxification of CEES vapors has not been studied on $Zn(OH)_2$/ZnO materials. The presence of a particular crystal structure might change the detoxification performance of a material, promoting a reactive adsorption of CEES or influencing a mechanism pathway.

Based on the above, the objective of this paper is an evaluation of the role of the structure and chemistry of zinc hydroxide and oxide as reactive adsorbents for CEES decontamination. The target is the reactive adsorption of Chemical Warfare Agents at ambient conditions and their conversion on the surface into less toxic compounds. In order to assess the photoactivity in visible light of the materials tested, the experiments were performed in the dark and under a light irradiation with a solar simulator. Owing to the target application of these materials in ambient conditions only photoactivity under a visible light irradiation has been explored. The comparison of two different crystal phases of the zinc (hydr)oxides (including a commercial zinc oxide) will provide information about the role of —OH groups and porosity in the reactive adsorption process. We hypothesize that an increase in the number OH surface groups will enhance a detoxification extent, chemical reactivity and photocatalytic degradation/oxidation of the mustard gas surrogate, CEES.

2. Experimental

2.1. Materials

All chemicals (Zinc chloride and sodium hydroxide) were reagent grade with a purity degree than 99%. Commercial NanoActive® Zinc Oxide (ZnO—C) was supplied by NanoScale Corporation. All solutions were prepared with deionized water.

The procedure for the synthesis of zinc hydroxide (ZnSA) was described previously [5]. Briefly, 1 L of a sodium hydroxide solution (0.05 M), was added to a 0.5 L of zinc chloride (0.05 M) solution, at a rate of 2.0 mL/min, using a Titronic Universal (SCHOTT) [15]. The obtained material was filtered and washed with distilled water until no trace of chloride was detected and the pH of the leachate was neutral. The solid was filtered and dried at 60 °C for 48 h. This methodology is referred to as a "slow addition" in the paper.

Zinc oxide (ZnRA) was prepared by a direct rapid addition of a 1.0 L sodium hydroxide solution (0.05 M) to a 0.5 L zinc chloride solution (0.05 M) and then aged for 2 h, which was accompanied by stirring. The obtained material was washed with distilled water until neutral pH and no traces of chloride ions were found. The filtrated phase was dried at 60 °C for 48 h. This methodology is referred to as a "rapid addition" in the paper.

2.2. Methods

2.2.1. CEES reactive adsorption

The reactive adsorption of CEES was studied in batch experiments. A glass vial containing 150 mg of a selected sample was placed in a 160 mL reaction vessel closed with a septum. The vessel was sealed hermetically and 300 μL of CEES were injected through the septum into a 5 mL beaker inside the reaction vessel. The containers were kept under a solar light simulator (Xenon lamp, solar light Co., Inc., XPS-150^{TM}) or in the dark, at room temperature, for 24 h. Then, the containers were opened and the adsorbent samples were left to equilibrate in dry air for 1 h at the atmospheric pressure. Finally, the containers with the adsorbents were weighed, and the mass gain as a result of adsorption was recorded.

2.2.2. FT-IR spectroscopy

Fourier transform infrared (FTIR) spectroscopy was carried out on a Nicolet Magna-IR 830 spectrometer using the attenuated total reflectance (ATR) method. The spectrum was generated and collected 64 times and corrected for background noise.

2.2.3. XRD

X-ray diffraction (XRD) measurements were conducted using powder diffraction procedures. Adsorbents were ground to powder size and then analyzed by a $Cu_{K\alpha}$ radiation generated in a Phillips X'Pert X-ray diffractometer.

2.2.4. Simultaneous thermal analysis-mass spectroscopy

Thermogravimetric curves (TG) were obtained using a TA Instruments Thermal Analyzer (New Castle, DE, USA). The heating rate was 10 °C/min from room temperature to 1000 °C. During the whole experiment a flow rate of 100 mL/min of ultra-purity helium was purged. The differential thermal (DTG) profiles were derived from the TG curves. Simultaneously, gases and vapors released with an increased temperature were analyzed with a ThermoStar Gas Mass Spectrometer (GSD; Pfeiffer Vacuum). The off-gas collected was scanned with a secondary electron multiplier detector and a Faraday detector. The m/z identified in the MS was correlated in real time with their corresponding releasing temperature and the m/z thermal profiles were obtained.

2.2.5. Potentiometric titration

Potentiometric titration measurements were performed with an automatic titrator (888 Titrando, Metrohm). The initial materials (~0.050 g) were added to $NaNO_3$ (0.01 M, 25 mL) and placed in a container maintained at 25 °C overnight for equilibrium. During the titration, the suspension was continuously saturated with N_2 to eliminate the interference of atmospheric CO_2. Volumetric standard NaOH (0.1 M) was used as a titrant starting from the initial material's pH up to pH 11. The experimental data was transformed into a proton-binding curve, Q, representing the total number of protonated sites [16,17]. The deconvolution of Q, using the SAIEUS procedure, [17] yield the pK_a distributions for the species present on the surface.

2.2.6. Adsorption of nitrogen

Nitrogen isotherms were measured using an ASAP 2020 (Micromeritics, Surface area and Porosity Analyzer Norcross, GA, USA) at −196 °C. The samples were outgassed at 120 °C to vacuum 10^{-4} Torr before the measurements. The surface area, S_{BET} (Brunauer–Emmet–Teller method was used), the micropore volume, V_{mic} (calculated using the Dubinin–Radushkevich approach), the mesopore volume, V_{mes}, and the total pore volume, V_t (calculated from the last point of the isotherms based on the volume of nitrogen adsorbed) were calculated from the isotherms. The volume of mesopores, V_{mes}, represents the difference between the total pore volume and the micropore volume.

2.2.7. SEM

Scanning electron microscopy images were obtained using a Zeiss Supra 55 VP with an accelerating voltage of 5.00 kV.

2.2.8. Ultraviolet–visible–near infrared (UV–vis–NIR) spectroscopy

The spectra were obtained in a Cary 500 Scan spectrometer (Varian) by using the Cary 500 diffuse reflectance accessory (integrated sphere). Before the analyses, the samples were compressed to form 0.55 mm thick pellets. The samples were mounted on a black tape and fitted into an integration sphere analysis port. The integration sphere was operated to collect diffuse reflection.

2.2.9. Mass extraction and MS–MS analysis

In order to qualitatively determine the products of the CEES reactive adsorption that are deposited on the materials' surfaces an extraction with acetonitrile was carried out. 50 mg of exhausted material was equilibrated with 5 mL of the extracting agent for 5 days. Then, the solution was filtrated and injected into a mass spectrometry system (Q-TRAP 400, Applied Biosystems). The MS parameters used were as follows: ion spray voltage, 5500 V (highest sensibility); collision energy, from 10 to 50 V depending on the molecular weight selected; collision energy spread, 40 V, and declustering potential, 80 V. Nitrogen gas was used as a curtain and collision gas.

3. Results and discussion

The identification of the crystal structure was carried out using the X-ray diffraction measurements. The XRD patterns of the ZnSA and ZnRA samples are shown in Fig. 1. In the sample synthesized at the slow rate (ZnSA) zinc hydroxide is the main crystallographic phase. The diffraction peaks of ZnSA at 20.2, 20.9, 27.2, 27.8, 32.9, 39.5, 40.8, 42.1, 52.4, 57.9, 59.5 and 60.4 2θ represent those of orthorhombic ϵ-$Zn(OH)_2$ (JCPDS 38-0385) [3]. Other minor diffraction peaks, located at 31.7, 34.4, 36.2 and 47.6, detected on the X-ray diffraction pattern of this sample correspond to traces of würtzite structure of zinc oxide (JCPDS 36-1451).

The rapid addition of NaOH to $ZnCl_2$ generates a pH gradient, which affects the crystal structure. As a result, the main crystallographic phase detected is that of zinc oxide. The diffraction peaks at 31.7, 34.4, 36.2 and 47.6 2θ correspond to würtzite. A minor presence of wülfingite (ϵ-$Zn(OH)_2$) crystals is also noticed. The pattern of the ZnO—C matches with the one of würtzite. The crystallite sizes

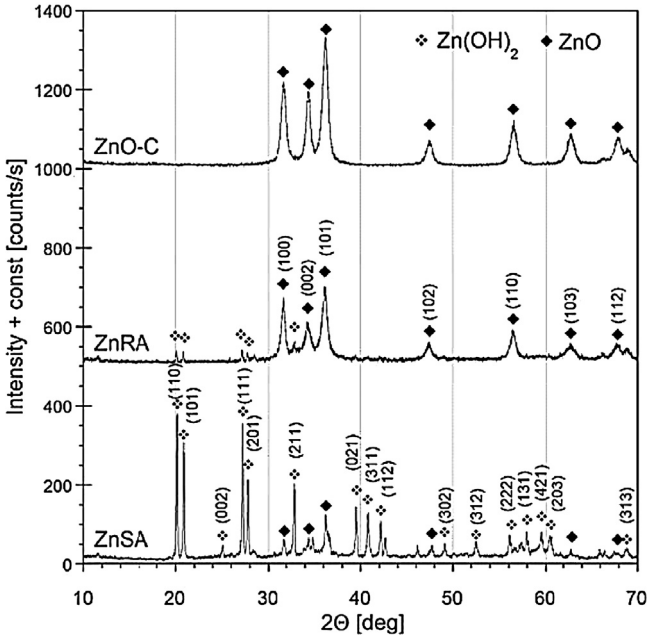

Fig. 1. X-ray diffraction patterns for the initial samples.

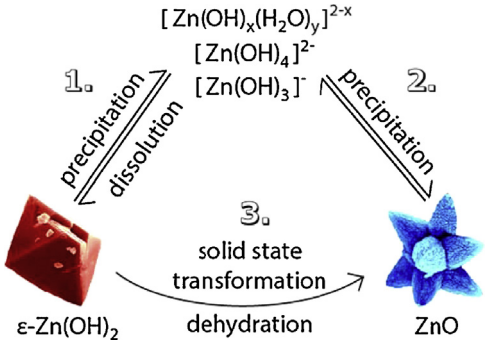

Fig. 2. Possible reaction pathways for the formation of $Zn(OH)_2$ and ZnO.

calculated using the Scherrer equations are 48.6, 11.8 and 15.1 nm for ZnSA, ZnRA and ZnO—C, respectively, as shown elsewhere [18].

The obtained results follow the previous findings that different precipitates are formed by changing the mixing time and thus the pH gradient [4,6]. For both synthesis procedures, the initial $ZnCl_2$/NaOH molar ratio was 0.5 and the initial pH of the precursor solution was 5.9 ± 0.2. The slow addition of the NaOH raises the solution pH to 9.4 ± 0.2. On the contrary, the rapid NaOH addition increases the pH to a higher value of 11.4 ± 0.2. Since the addition of NaOH to the zinc precursor solution causes the formation of $[Zn(OH)_4]^{2-}$, $[Zn(OH)_3]^{-1}$, and $[Zn(OH)_x(H_2O)_y]^{2-x}$ intermediate aquo-complexes [2,4], the synthesis of either $Zn(OH)_2$ or ZnO depends on the kinetics of the precipitation and can be controlled by the pH value. With the slow NaOH addition, the pH was always maintained lower than 10 through the whole synthesis procedure. In such a system, the $[Zn(OH)_4]^{2-}$, $[Zn(OH)_3]^{-1}$ and $[Zn(OH)_x(H_2O)_y]^{2-x}$ complexes condensed, resulting in the formation of zinc hydroxide. Under these particular conditions (room temperature, precursor concentration, and pH between 6.5 and 10), the precipitation of stable $Zn(OH)_2$ is favorable over that of ZnO. On the contrary, with the rapid NaOH addition, the pH suddenly increased to higher than 10.8. It is likely that initially $Zn(OH)_2$ and ZnO were formed simultaneously. Then, $Zn(OH)_2$ was transformed to ZnO via two possible pathways [2]. The first could involve a dissolution to the aforementioned complexes [18] followed by a re-precipitation to ZnO (Fig. 2), which is less soluble and more stable in the whole pH range [4]. The second pathway could be based on a solid-state transformation caused by dehydration (Fig. 2). This mechanism is in agreement with results reporting the synthesis and transformation of ZnO by the decomposition of $Zn(OH)_2$ [2,3,6,19].

The FTIR spectra are presented in Fig. 3. The spectrum for ZnSA reveals bands at 715 and 900 cm^{-1} that are assigned to the out-of-plane bending and vibration modes of the OH groups [5]. The band detected at 830 cm^{-1}, is assigned to the —OH deformation, and the ones at 1040 and 1090 cm^{-1} are assigned to the Zn—OH bending and twisting, respectively [2,20]. The band at 1390 cm^{-1} (with a small shoulder at 1360 cm^{-1}) and the band at 1500 cm^{-1} are assigned to vibrations of OH bonded to zinc hydroxide and water. While the broad band between 3000 and 3300 cm^{-1} is assigned to bulk OH groups and the one at 3450 cm^{-1} to water molecules [2], the band at 3450 cm^{-1} represents the OH groups of water molecules.

The FTIR spectrum of ZnRA showed a different pattern. The bands of the $Zn(OH)_2$ bending and twisting vibrations are absent. The bands from the out-of-plane bending and vibration modes of the OH groups at 715 and 900 cm^{-1} decreased significantly in their intensities, and a broad band appeared between 800 and 1000 cm^{-1}. The same decreasing trend was found in the broad band between 3000 and 3300 cm^{-1}. Furthermore, the band representing water at 3450 cm^{-1} also decreased in its intensity. These results are in agreement with the ones reported by Nicholas et al. for ZnO

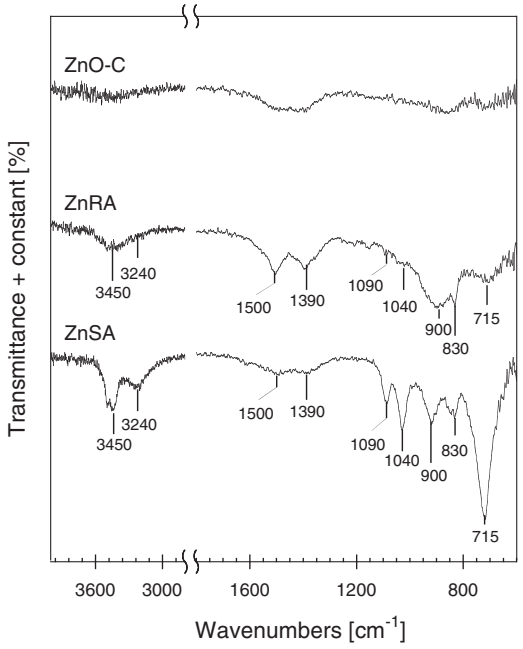

Fig. 3. FTIR spectra for the ZnSA, ZnRA and ZnO—C samples.

synthesized from the thermal decomposition of ϵ-$Zn(OH)_2$, (obtained in ammonium hydroxide) where the final pH of the solution was close to 11 [2]. As seen from the FTIR results, the spectrum for ZnRA clearly lost most of the signals related to the OH groups. The bands related to the hydroxyl groups and/or water molecules were absent in the ZnO—C.

The amount of functional groups on the surface was determined using the potentiometric titration method. The pK_a distributions for the species present on the surface of our materials are collected in Fig. 4. Two kinds of functional groups are identified: those with pK_a between 7 and 8, and those with pK_a higher than 10. The first ones are linked to oxygen bridging groups, and the second ones to hydroxyl terminal groups [21]. The higher pK_a of the terminal groups for ZnSA than those for ZnRA indicates more basic character of these groups on the former sample, which is probably caused by their different chemical environment related to the discussed above higher level of amorphicity. The results clearly show that the amount of both types of groups is higher on the surface of ZnSA than

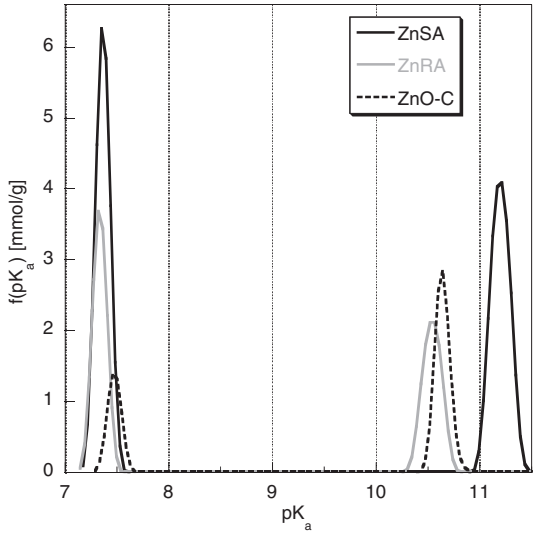

Fig. 4. pK_a distributions for the samples studied.

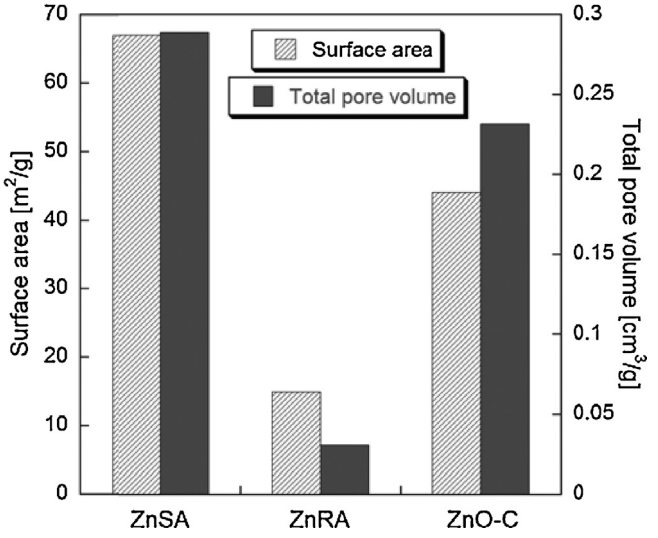

Fig. 5. Comparison of the parameters of the porous structure calculated from the nitrogen adsorption isotherms.

on that of ZnRA. The terminal hydroxyl groups of ZnRA represent only 29% of the groups on ZnSA. Also, on the surface of the former sample there are 57% less bridging groups than those on the surface of ZnSA. For the commercial zinc oxide, the numbers of the terminal and the bridging groups are 62 and 84% smaller, respectively, in comparison to those detected on ZnSA.

Besides the structure and morphology, ZnSA and ZnRA differ markedly in their pore structure. The surface area and the total pore volume are summarized in Fig. 5. ZnSA has 350% higher surface area than that of ZnRA. Both materials were found to be mesoporous, with ZnSA having a six times higher total pore volume than that of ZnRA. This mesoporous nature of our samples is important and might play a significant role in the CEES reactive adsorption process [22,23]. The ZnO—C has also a mesoporous structure, with the total pore volume 13% lower than that of ZnSA. Its surface area is 44 m^2/g.

The SEM images of ZnSA (Fig. 6A) show the well crystallized micrometric size particles of ϵ-$Zn(OH)_2$ with the rhombic octahedral shape of zinc hydroxide [4,6,24]. Platelets-like particles of similar sizes, which correspond to the zinc oxide phase, are also found on the SEM images in a limited quantity (Fig. 6B). In the case of ZnRA, flower-like zinc oxide particles with a size of about 500–1200 nm are the predominant crystallographic phase, which is in agreement with the XRD results (Fig. 6C). Besides the oxide phase, the well crystallized rhombic octahedral shape particles of ϵ-$Zn(OH)_2$ were also detected, which are the minor phase in ZnRA (Fig. 6D).

The UV–vis–NIR absorption spectra of the samples are presented in Fig. 7A. ZnRA displayed a higher adsorption of photons in the whole electromagnetic spectrum. The absorbance has a semiconstant value in the visible range, and as the wavelength approaches the UV range, the absorption dramatically increases, reaching a peak at a wavelength close to 340 cm^{-1}. The absorption spectrum of ZnSA follows the same pattern, but the band at 350 cm^{-1} is much less intense. From the UV–vis–NIR spectra, the band gaps of the materials were calculated. Details of the calculation are reported elsewhere [22]. Briefly, the extrapolation of the linear fit of the plot of $[F(R_\infty)\,h\nu]^2$ versus the photon energy ($h\nu$) yields the value of the energy band gap (E_g). The plots are provided in Fig. 7 B. The E_g of ZnSA, ZnRA and ZnO—C is 3.22 eV, 3.05 eV and 2.98 eV, respectively. While the E_g of ZnRA and ZnO—C are in the range of other ZnO materials reported in the literature [25], the ZnSA band gap energy represents a typical value found for zinc (hydr)oxides [26,27]. A wide band gap feature is an advantage of our materials,

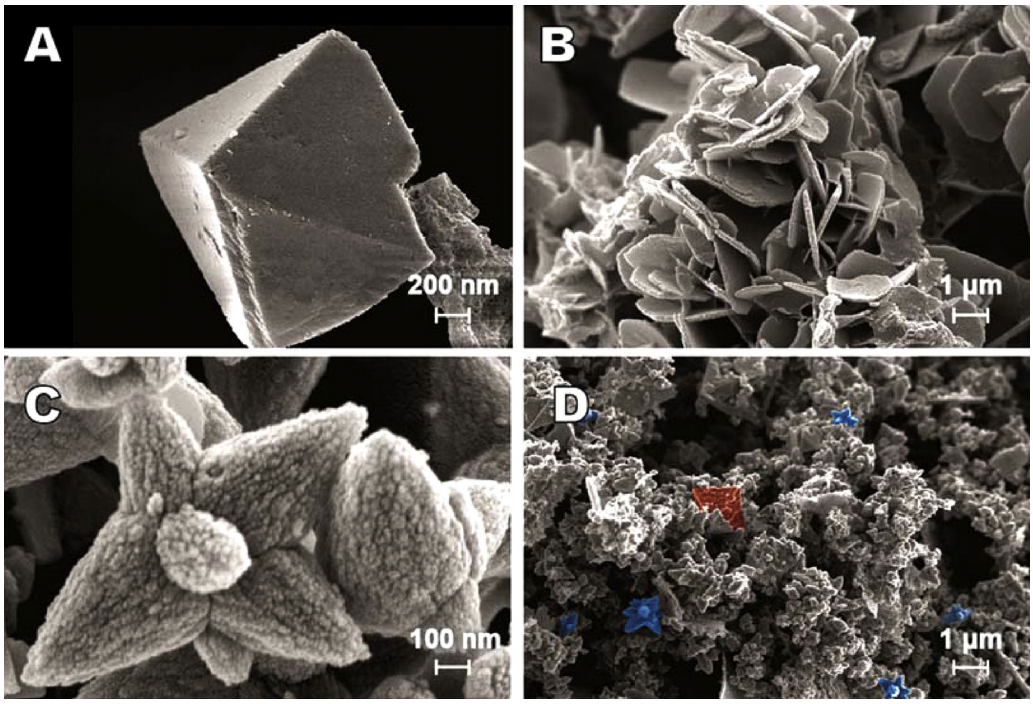

Fig. 6. SEM images of ZnSA (A, B) and ZnRA (C, D). Red (false) color the ϵ-$Zn(OH)_2$ particles and Blue (false) color- the ZnO nano-flower like particles. (For interpretation of the references to colour in this figure legend, the reader is referred to the web version of this article.)

since this characteristic is beneficial for the development of optical and electronic devices [28].

The synthesized materials were used as CEES adsorbents and an increase in the weight after 24 h of the CEES exposure was recorded. The weight increase represents the capacity (Q_{ads}) of the samples to retain CEES and/or its reaction products. The results obtained with the solar simulator (L) and in the dark (D) are shown in Table 1.

ZnSA has a higher adsorption capacity than that of ZnRA, in both light (263% increase) and dark (120%) conditions. However, an increase in the uptake in light was recorded only for ZnSA, indicating higher photoactivity compared to ZnRA. On the commercial zinc oxide, the measured CEES capacity under the light exposure was 29 mg/g. Even though it is only half of the capacity measured on ZnSA, it is almost double than that of ZnRA. As in the case of ZnRA, the capacities in light and the dark measured on ZnO—C were comparable.

Knowing the differences in surface chemistry, these results suggest an important role of the OH groups of ZnSA not only in the extent of the adsorption process but also in the extent of photoactivity. The relationship between the CEES adsorption capacity and the number of terminal hydroxyl groups shows a linear trend with $R^2 = 0.97$ (Fig. 8). Moreover, the dependence of the capacity on the surface area also shows a linear trend, however, the correlation is weaker ($R^2 = 0.92$). In the analysis of these data, we have to take into

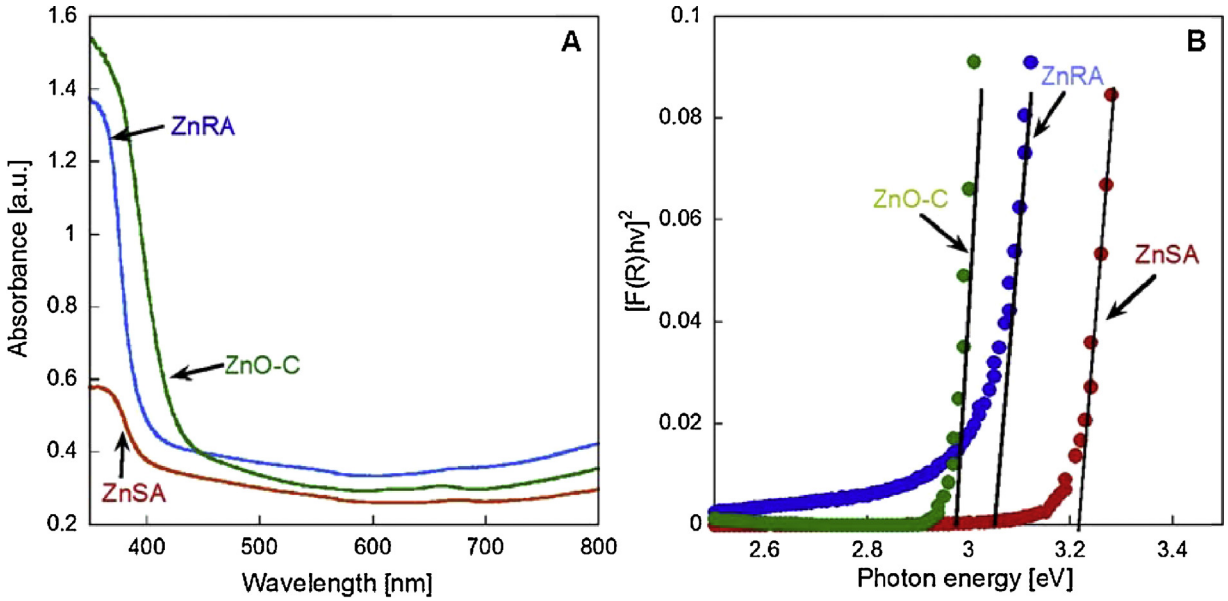

Fig. 7. (A) UV–vis–NIR spectra of the samples, (B) $[F(R_\infty)\,h\nu]^2$ versus photon energy. The lines show the cut-off used to calculate the band gab energy.

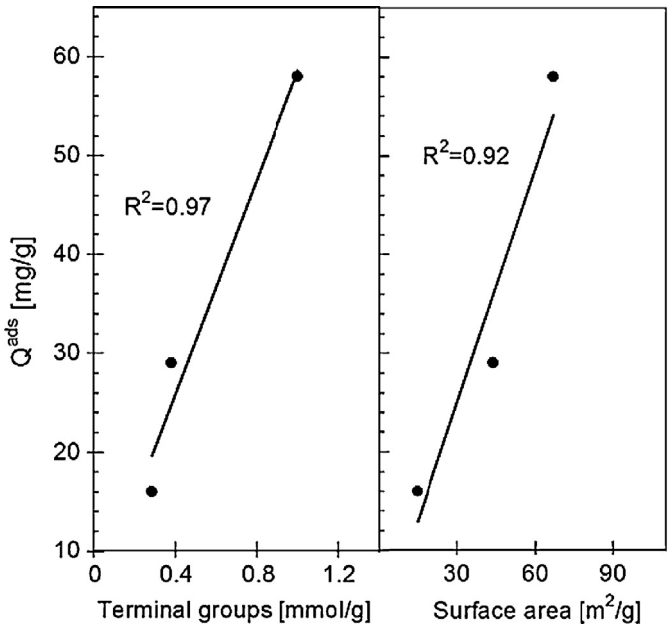

Fig. 8. Dependence of the amount adsorbed on the terminal groups (left) and the surface area (right) under the light exposure.

Table 1
Adsorption capacities measured under the light exposure from the solar simulator (L) and at the dark (D).

	Q^{ads} (mg/g)	
Sample	*L*	*D*
ZnSA	58	33
ZnRA	16	15
ZnO—C	29	30

account that the higher number of functional groups must be naturally associated with a higher surface area, which in turn is related to the degree of surface amorphicity. Nevertheless, these results indicate the importance of terminal OH groups for the CEES retention on the surface of the materials studied. Bandosz et al. reported the positive role of terminal OH groups during the reactive vapor adsorption of actual chemical warfare agents (CWAs) on zirconium hydroxide [29]. The loss of the terminal hydroxyl groups upon calcination from dehydration and dehydroxylation led to a decrease in the reactivity toward the CWAs.

Thermal analysis results were used to further evaluate the nature of the degradation products and surface reactivity of our materials. DTG curves are presented in Fig. 9. The DTG curve for the initial ZnSA sample reveals a peak at 140 °C, which is assigned to the removal of physically adsorbed water (7.9%). The peak at 226 °C is linked to the dehydration of $Zn(OH)_2$, causing an additional 8.9% weight loss [24]. The shoulder at about 450 °C can be attributed to the dehydroxylation process [30] which results in a 6.1% decrease in the weight. The total weight loss of ZnSA was 23.2%. The pattern of the DTG curve for ZnRA differs from the one for ZnSA. The small weigh loss of 0.9% below 140 °C suggests a marked hydrophobicity. Also, the small weight losses at 240 °C and 430 °C that were previously attributed to the dehydration and dehydroxylation, respectively, indicate the limited amount of hydroxyl groups on the surface. The total weight loss for this sample was 3.9%. The total weight loss for ZnO—C was only 2.9% due to the absence of the dehydration and dehydroxylation in the ZnO phase.

After the CEES exposure in light, the DTG curve for the ZnSA sample shows three new peaks at 160 °C, 300 °C, and at the temperature higher than 760 °C. The MS thermal profiles of species present in the

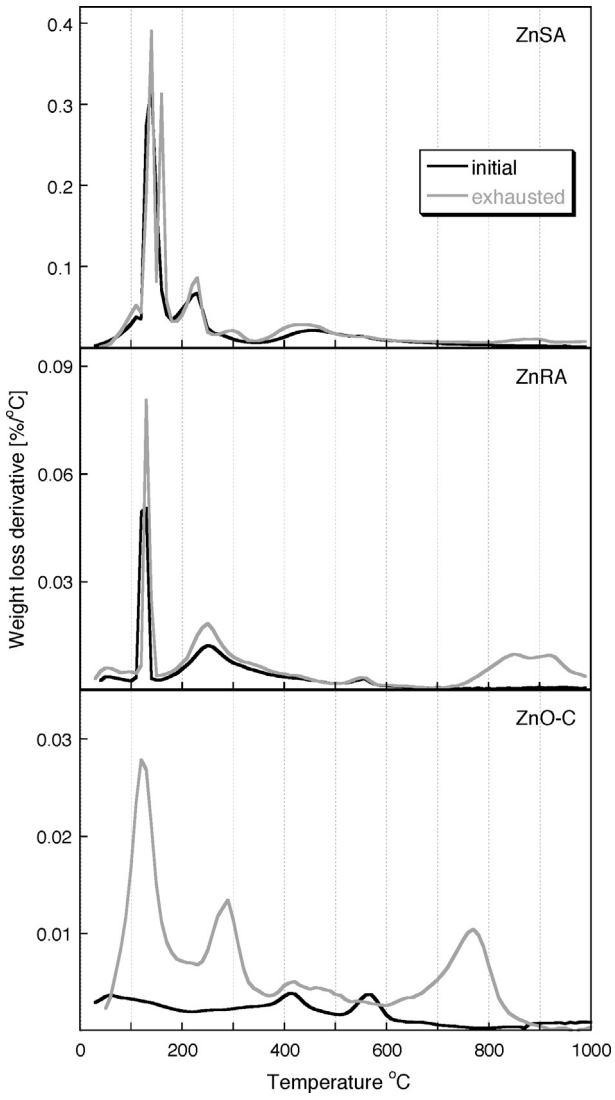

Fig. 9. DTG curves in helium for ZnSA, ZnRA and ZnO—C.

exhaust gases/vapors are collected in Fig. 10. The MS thermal profiles indicate that the first peak at 160 °C is related to the removal of EVS and CEES (*m*/*z*: 88,73, 60, 59, 27) [31] from the material's surface. The peak at 300 °C can be assigned to the decomposition of the strongly adsorbed CEES and/or HEES [32,33]. Finally, the weight loss that occurred above 760 °C is linked to the removal of $ZnCl_2$ species [34] and/or to the reduction of zinc oxide to Zn (boiling point 907 °C) by the carbonaceous phase [8]. The traces of the latter phase might be formed during the thermal analysis (charring of organic compounds). The total weight loss of the exhausted ZnSA sample in light was 28.3 wt.%. The difference in the total weight loss between the initial and exhausted sample is 5.1 wt.%, which is in good agreement with the amount adsorbed (Table 1).

The DTG curve of the exhausted ZnSA sample in the dark does not reveal any peak at 160 °C and in fact on this sample EVS was not detected by the MS analysis. These results suggest that exposure to light promotes the transformation/elimination reaction of CEES to EVS during their reactive adsorption on ZnSA.

On the other hand, for ZnRA the differences on the DTG curves between the initial and exhausted samples are less pronounced than those for ZnSA. An increase in the intensity of the 160 °C peak on the exhausted in the light sample's DTG is linked to the formation of EVS, and the shoulder at the 330 °C is related to the removal of CEES. The broad peak above 780 °C is attributed to the

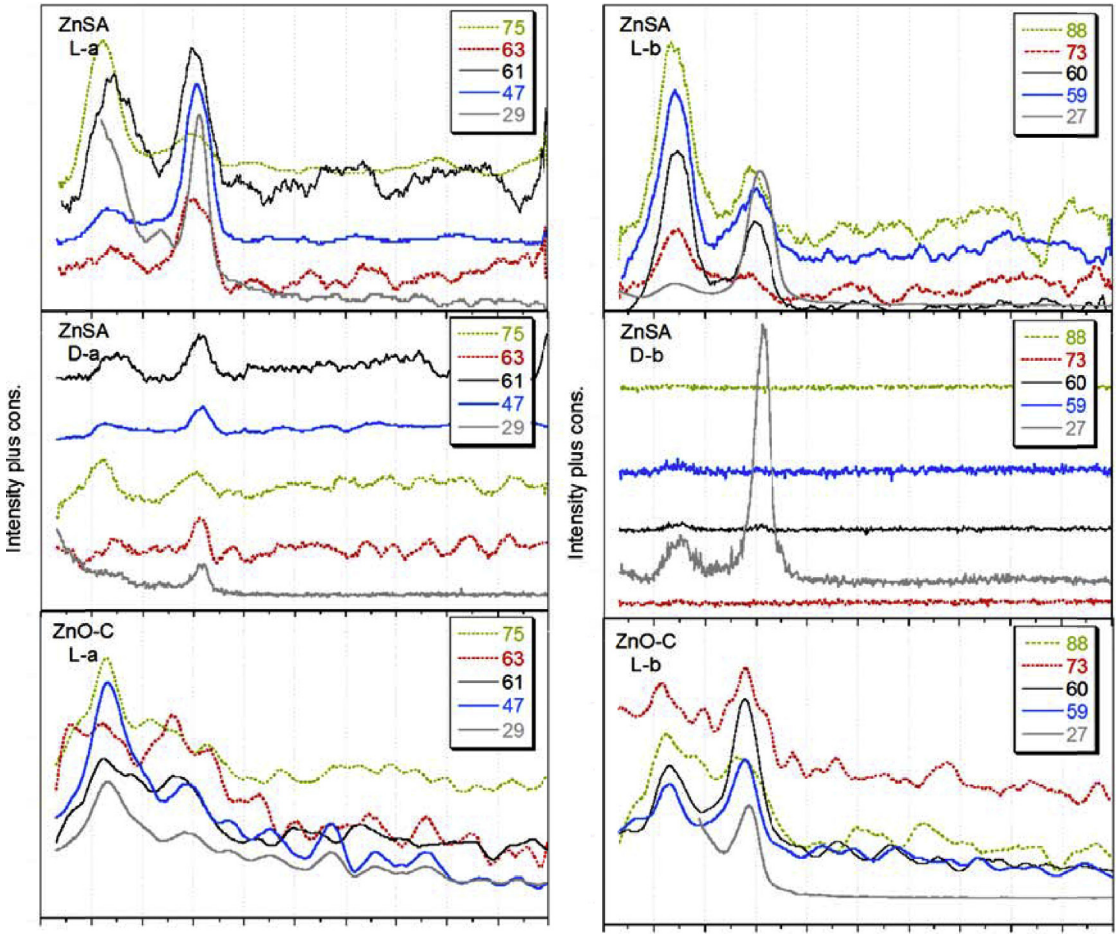

Fig. 10. MS thermal profiles (in helium) for the fragments related to CEES and/or HEES (a) and EVS (b) for the ZnSA exhausted sample in the light (L) and in the dark (D) and for the ZnO—C in light (L).

reduction of zinc oxide to Zn by the carbonaceous phase formed during heating with the organic species adsorbed on the surface at inert atmosphere. This peak can be also attributed to the removal of $ZnCl_2$ [34], indicating the direct reaction of the Zn ions with the Cl^- ions. The difference in the weight loss between initial and exhausted ZnRA is 1.4 wt.%.

The DTG curve of the exhausted ZnO—C shows the same peaks as those on the exhausted ZnRA sample, however they are shifted to slightly lower temperatures. The analysis of the *m*/*z* thermal profiles (Fig. 10), indicates that these peaks are the same as those detected in the DTG of the ZnSA. This is an indication that EVS and CEES are present on the surface, although in a minor amounts, due to the limited adsorption on this sample. The total weight loss on ZnO—C exposed to CEES is 2.5% larger than that of the initial sample. Owing to the small amount of CEES adsorbed on ZnRA and the limits in the sensitivity of the MS detector, only the MS thermal profiles for ZnSA and ZnO—C are presented and discussed. In order to further elucidate the mechanism of CEES interactions with the surface of our materials, the extracts of the species removed from the surface were analyzed by MS–MS. The main compound detected for the ZnRA, ZnSA and ZnO—C samples while exposed to light is ethyl vinyl sulfide (EVS). However, in the extract from ZnSA, 2-hydroxyethyl ethyl sulfide (HEES) was also present. This indicates the key role of the hydroxyl groups during CEES reactive adsorption, which leads to the formation the hydrolysis product. No trace of CEES was found in any of the exhausted samples. Since the CEES presence was supported by the TA-MS analyses, its absence during the analysis of the extracts indicates the inability of acetonitrile to

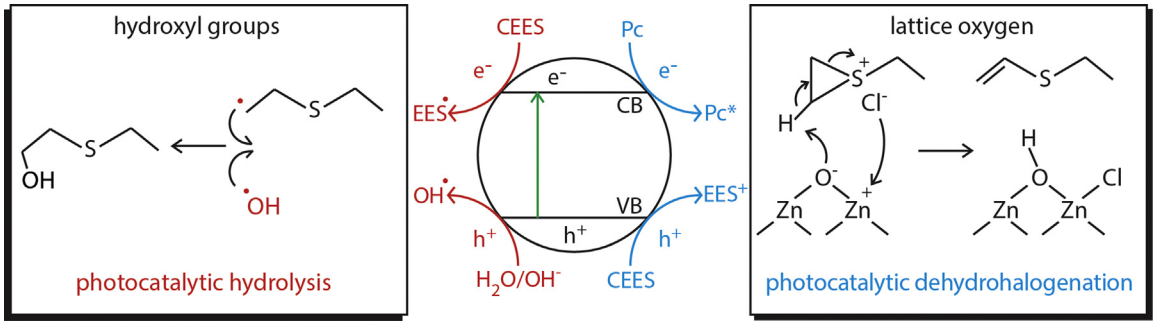

Fig. 11. Proposed reactions scheme of CEES reactive adsorption upon the visible light exposure.

Table 2
Highlighted studies about the HD and/or CEES removal on different metal based materials.

Material	Conditions	Observations	Reaction products	Ref.
Cu-BTC MOF	Liquid HD and CEES in carbon tetrachloride.	The degradation of CEES and the production of byproducts are dependent on the porous structure and reactive sites. The removal kinetics follows the first order reaction; the maximum CEES capacity: 92 mg/g.	TDG HEES	[53]
CuO nanoparticles calcined	Direct interaction of powder with HD (liquid HD).	The capacity: 47 mg/g; the adsorption capacity and the nature degradation products depend on the calcination temperature, which affects the surface area.	TDG, DVS, HEVS, VCES	[54]
MgO nanoparticles	Liquid CEES in heptane, methanol pentane, and tetrahydrofuran.	Surface area and crystal shape affect the decontamination; solvent enhances dramatically the uptake; the capacity: 30 mg/g. The highest reaction rates obtained with pentane as a solvent.	EVS HEES	[31,55]
Porous vanadium oxide nanotubes	Direct interaction of powder with CEES and liquid phase degradation in pentane.	In the liquid phase the degradation is faster than that without a solvent; the calculated capacity: 45 mg/g.	HEES, sulfoxide, VES	[23]
ZnO nanosized rods and commercial ZnO	Liquid HD in chloroform.	ZnO nanorods were more efficient in degradation than the commercial bulk ZnO, although they have almost the same surface area (52 and 40 m^2/g, respectively); the capacities: 20–25 mg/g after 48 h.	TDG, DVS	[43]
Manganese oxide nanoblets	Liquid HD and CEES in dichloromethane.	The nanobelts hydrolyzed CWA; the capacities: 25–40 mg/g.	DTG and HEES	[33]
Titanium oxide	Gas CEES	26 Compounds extracted from the surface after the adsorption in UV; in dark, only seven detected.	26 compounds	[36]
Zinc hydroxide/zinc oxide	Vapors of CEES under visible light.	Dependence of the CEES removal capacity on the amount of terminal hydroxyl groups and surface area; capacity: 58 mg/g.	EVS HEES	This study

Abbreviations: thiodiglycol (TDG), hydroxyethyl ethyl sulfide (HEES), divinyl sulfide (DVS), hydroxyethyl vinyl sulfide (HEVS), vinyl chloroethyl sulfide (VCES), ethyl vinyl sulfide (EVS), vinyl ethyl sulfide (VES) and divinyl sulfide (DVS).

extract CEES from the materials. It suggests a strong adsorption of CEES on our samples. EVS was detected only in the samples exposed to light, implying that photocatalytic reactions are involved in its formation. This also indicates that in the absence of light CEES was adsorbed only in the unchanged form.

It is important to mention that HEES that is the hydrolysis/oxidation product was only detected in the extract from ZnSA. No other oxidation products such as thiodiglycol, diethyl sulfoxide or diethyl sulfone were found in the extracts for both ZnSA and ZnRA samples. The latter compounds have been reported as the degradation products of the CEES/HD [35–37]. In this study, their lack demonstrates the favorable formation of EVS on our materials under the visible light exposure.

It is well known that zinc oxide is photoactive in visible light [25,28,38–40]. The band gaps for both materials synthesized in this study support their photoactive properties. As expected, the higher surface area of ZnSA increased the capacity for adsorption especially owing to the high dispersion of the terminal OH groups on the surface. The results obtained indicate that these groups play a crucial role on the extent of adsorption and the degree of CEES transformation.

Our materials can act as a photocatalyst (Pc), absorbing a photon, which leads to the excitation of the photocatalyst (Pc*):

$$Pc + h\nu \rightarrow Pc* \quad (1)$$

The excited surface of the photocatalyst uses the energy for a primary photocatalytic reaction. Therefore, after being adsorbed (most likely by hydrogen bonds [41]), CEES is transformed into ethyl ethyl sulfonium (EES) cation by means of a Photoinduced Electron Transfer (PET) reaction [33,42]:

$$Pc* + CEES \rightarrow Pc^- + EES^+ \quad (2)$$

It has been reported that once EES^+ is formed, it may be converted to a cyclic cation through an intermolecular cyclization process [33,43–46]. After that, a labile hydrogen from the cation transfers to the negative charged lattice oxygen of the zinc phase, that acts like a Lewis base [47,48]. This proceeds via an bimolecular elimination (E2) pathway, results in the formation of the dehydrohalogenation vinylic product, EVS [36,49]. Simultaneously, the chloride anion reacts with a zinc atom on the surface forming $ZnCl_2$. Zafrani et al. reported that the main degradation product of anhydrous HD on Al_2O_3 was VVS [50]. In our study, EVS was detected on the ZnSA and ZnRA samples only after the CEES exposure at the light.

When hydroxyl groups and/or physisorbed water molecules are present, the CEES transformation can proceed by a substitution of the Cl^- ion by the OH group [45]. The crucial role of water has been reported for CaO [51]. Absorption of a photon excites the electron from the valence to the conduction band of $Zn(OH)_2$. The formed holes react with water associated with the hydroxyl groups in the zinc hydroxide phase, resulting in the formation of hydroxyl radicals [11]. S-CH_2CH_2Cl is destabilized by the electron/hole pair and gets transformed into a transient radical. The latter reacts with the hydroxyl radical that acts as an nucleophile, producing the hydrolysis product, HEES [36]. It remains on the surface probably by physical interactions, such as hydrogen bonding. Since water, light and thus formation of OH radicals are crucial for this process, HEES was formed and detected only on the ZnSA sample exposed to light. Other studies have also shown that the terminal groups participated in photochemical reactions via the formation of hydroxyl radicals, therefore enhancing the removal of sulfide species such as CEES [45] or H_2S [11. The rate-determining step is the transformation of the cations to HEES, which is enhanced by light [44,45]. The same pathways were proposed by Martyanov and Klabunde on TiO_2 [35], and Singh et al. on vanadium oxide [23], where large amount of water and isolated hydroxyl groups contributed to the formation of HEES. Furthermore, Zafrani et al. reported that on Al_2O_3 in the presence of water HD was degraded to thiodiglycol instead to divinyl sulfide [50]. In our study, hydroxyl groups and associated with them water lead to the formation of HEES on ZnSA upon the light exposure. It is worth to mention, that the two degradation products obtained on our materials are considerably less toxic than is the CWA surrogate used in this study. Based on the results obtained, a schematic representation of reaction pathways on the surface of our materials is proposed (Fig. 11).

A direct comparison of the performance of our materials as CEES reactive adsorbents to those addressed in the literature is difficult due to the differences in the particular experimental setups

used. The summary of the results is presented in Table 2. As seen, the removal capacity on our materials is in the range of those reported on other metal oxides. However, the advantage of our samples is the photoactivity under visible light resulting in the detoxification of CEES. Even though the photocatalytic detoxification of CWA surrogates as CEES dimethyl methylphosphonate (DMMP), diethyl phosphoramidate (DEPA), pinacolyl methylphosphonate (PMP), butylaminoethanethiol (BAET) have been studied in aqueous suspensions of TiO_2 by Vorontsov, this material has been reported to be only active in the UV range [52]. Finally, an important aspect of the present work was addressing the paramount role of the terminal hydroxyl groups of the metal (hydr)oxide for the reactive adsorption of CEES. They affect the performance either in the dark or in light, although the roles they play differ.

4. Conclusions

The results presented in this paper show that by controlling the addition rate of a precipitation agent (NaOH) to a zinc salt solution, either zinc oxide or zinc hydroxide can be obtained. Slow rate results in the formation of orthorhombic particles of $Zn(OH)_2$, while a rapid addition leads to the formation of flower-like ZnO nanoparticles. The amounts of bridging and terminal hydroxyl groups and the surface area of $Zn(OH)_2$ were much higher than those of both synthesized and commercial ZnO. The presence of the hydroxyl groups causes a widening of the band gap in the materials studied. The surface of zinc hydroxide is more reactive toward 2-Chloroethyl ethyl sulfide (CEES) than that of zinc oxide owing to the crucial role of the OH groups in the hydrolysis reactions. Moreover, the developed surface area increases the number of active sites on the adsorbent, allowing their interactions/reaction (lattice oxygen and hydroxyl groups) with the organic molecules. Even though ethyl vinyl sulfide was identified as the main degradation product on both materials when the experiments were performed in light, hydroxyethyl ethyl sulfide (HEES) was only formed on zinc hydroxide. It is hypothesized that the CEES degradation is triggered by the excitation of the zinc hydroxide phase by photons. This, besides forming OH radicals from adsorbed water, leads to the formation of the ethyl ethyl sulfide cation. That cation is transformed via dehydrohalogenation to the vinylic product ethyl vinyl sulfide (EVS) after the reaction with lattice oxygen. When hydroxyl groups are present, the EES radical reacts with hydroxyl radicals, leading to the formation of HEES. No CEES degradation products were detected on the surface when the experiments were run in the dark. Thus the enhancement in the adsorption capacity as well as the identification of HEES and EVS as the degradation products formed upon the light exposure support the photoactivity.

Acknowledgements

This study was supported by the ARO (Army Research Office), USA grant W911NF-10-1-0030 and W911NF-13-1-0225 and NSF collaborative SBET Grant No. 1133112. The assistance of Dr. Jorge Morales in SEM studies is appreciated.

References

[1] J. Zhang, Chem. Mater. 14 (2002) 4172.
[2] N.J. Nicholas, G.V. Franks, W.A. Ducker, CrystEngComm. 14 (2012) 1232.
[3] J. Wang, C. Liu, L. Xiang, J. Nanomater. (2013) 1.
[4] L. Yang, L. Xiang, J. Nanomater. 2013 (2013) 1.
[5] D.A. Giannakoudakis, T.J. Bandosz, J. Colloid Interface Sci. 436 (2014) 296.
[6] F. Giovannelli, A. Ngo Ndimba, P. Diaz-Chao, M. Motelica-Heino, P.I. Raynal, C. Autret, F. Delorme, Powder Technol. 262 (2014) 20.
[7] S. Yamabi, H. Imai, J. Mater. Chem. 12 (2002) 3773.
[8] M. Seredych, O. Mabayoje, M.M. Koleśnik, V. Krstić, T.J. Bandosz, J. Mater. Chem. 22 (2012) 7970.
[9] G. Kenanakis, Z. Giannakoudakis, D. Vernardou, C. Savvakis, N. Katsarakis, Catal. Today 151 (2010) 34.
[10] O. Mabayoje, M. Seredych, T.J. Bandosz, Appl. Catal. B 132–133 (2013) 321.
[11] M. Seredych, O. Mabayoje, T.J. Bandosz, Langmuir 28 (2012) 1337.
[12] M. Seredych, T. Bandosz, J. Phys. Chem. C (2010) 14552.
[13] B. Levasseur, A.M. Ebrahim, T.J. Bandosz, Langmuir 27 (2011) 9379.
[14] T.C. Marrs, R.L. Maynard, F.R. Sidell, Chemical Warfare Agents: Toxicology and Treatment, second ed., John Wiley & Sons, West Sussex, 2007.
[15] A. Bagreev, S. Katikaneni, S. Parab, T.J. Bandosz, Catal. Today 99 (2005) 329.
[16] J. Jagiello, Langmuir 10 (1994) 2778.
[17] J. Jagiello, T.J. Bandosz, J.A. Schwarz, Carbon 32 (1994) 687.
[18] G. Kyzas, N. Travlou, O. Kalogirou, E. Deliyanni, Materials 6 (2013) 1360.
[19] S. Mukhopadhyay, P.P. Das, S. Maity, P. Ghosh, P.S. Devi, Appl. Catal. B 165 (2015) 128.
[20 O. Srivastava, E. Secco, Can. J. Chem. 45 (1967) 579.
[21] P.W. Schindler, W. Stumm, Aquatic Surface Chemistry: Chemical Processes at the Particle–Water Interface, in: W. Stumm (Ed.), John Wiley & Sons, New York, 1987, pp. 83–110.
[22] J. Arcibar-Orozco, T. Bandosz, J. Mater. Chem. A 3 (2015) 220, http://dx.doi.org/10.1039/C4TA04159C.
[23] B. Singh, T.H. Mahato, A.K. Srivastava, G.K. Prasad, K. Ganesan, R. Vijayaraghavan, R. Jain, J. Hazard. Mater. 190 (2011) 1053.
[24 X. Qu, D. Jia, J. Cryst. Growth 311 (2009) 1223.
[25] V. Srikant, D.R. Clarke, J. Appl. Phys. 83 (1998) 5447.
[26] S.Z. Islam, T. Gayen, M. Seredych, O. Mabayoje, L. Shi, T.J. Bandosz, R. Alfano, J. Appl. Phys. 114 (2013) 043522.
[27 S.M.Z. Islam, T. Gayen, A. Moussawi, L. Shi, M. Seredych, T.J. Bandosz, R. Alfano, Opt. Lett. 38 (2013) 962.
[28] C. Klingshirn, J. Fallert, H. Zhou, J. Sartor, C. Thiele, F. Maier-Flaig, D. Schneider, H. Kalt, Phys. Status Solidi B 247 (2010) 1424.
[29] T.J. Bandosz, M. Laskoski, J. Mahle, G. Mogilevsky, G.W. Peterson, J.A. Rossin, G.W. Wagner, J. Phys. Chem. C 116 (2012) 11606.
[30] C. Wöll, Prog. Surf. Sci. 82 (2007) 55.
[31] B. Maddah, H. Chalabi, Int. J. Nanosci. Nanotechnol. 8 (2012) 157.
[32] R. Ramaseshan, S. Ramakrishna, J. Am. Ceram. Soc. 90 (2007) 1836.
[33] T.H. Mahato, G.K. Prasad, B. Singh, K. Batra, K. Ganesan, Microporous Mesoporous Mater. 132 (2010) 15.
[34] W.M. Haynes, CRC Handbook of Chemistry and Physics, 91st ed., Taylor & Francis, Boca Raton, 2010.
[35] I.N. Martyanov, K.J. Klabunde, Environ. Sci. Technol. 37 (2003) 3448.
[36] A.V. Vorontsov, C. Lion, E.N. Savinov, P.G. Smirniotis, J. Catal. 220 (2003) 414.
[37 P. Ramacharyulu, J. Kumar, J. Sci. Ind. Res. 73 (2014) 308.
[38] D. Li, H. Haneda, Chemosphere 51 (2003) 129.
[39] R. Ullah, J. Dutta, J. Hazard. Mater. 156 (2008) 194.
[40] C. Shifu, Z. Wei, Z. Sujuan, L. Wei, Chem. Eng. J. 148 (2009) 263.
[41] D. Panayotov, J.T. Yates Jr., J. Phys. Chem. B 107 (2003) 10560.
[42] A.V. Vorontsov, P.G. Smirniotis, Environmentally Benign Photocatalysts: Applications of Titanium Oxide-Based Materials, 1st ed., Springer, New York, 2010, pp. 579–621.
[43] G.K. Prasad, T.H. Mahato, B. Singh, K. Ganesan, P. Pandey, K. Sekhar, J. Hazard. Mater. 149 (2007) 460.
[44] S.Y. Bae, M.D. Winemiller, J. Org. Chem. 78 (2013) 6457.
[45] Y. Yang, L. Szafraniec, J. Org. Chem. 53 (1988) 3293.
[46] A. Kleinhammes, G.W. Wagner, H. Kulkarni, Y. Jia, Q. Zhang, L.-C. Qin, Y. Wu, Chem. Phys. Lett. 411 (2005) 81.
[47] T.H. Mahato, G.K. Prasad, B. Singh, J. Acharya, A.R. Srivastava, R. Vijayaraghavan, J. Hazard. Mater. 165 (2009) 928.
[48] D.B. Mawhinney, J.A. Rossin, K. Gerhart, J.T. Yates Jr., Langmuir 15 (1999) 4789.
[49] D. Panayotov, D. Paul, J. Yates, J. Phys. Chem. B 107 (2003) 10571.
[50] Y. Zafrani, M. Goldvaser, S. Dagan, L. Feldberg, D. Mizrahi, D. Waysbort, E. Gershonov, I. Columbus, J. Org. Chem. 74 (2009) 8464.
[51] G.W. Wagner, O.B. Koper, E. Lucas, S. Decker, K.J. Klabunde, J. Phys. Chem. B 104 (2000) 5118.
[52] A.V. Vorontsov, L. Davydov, E.P. Reddy, C. Lion, E.N. Savinov, P.G. Smirniotis, New J. Chem. 26 (2002) 732.
[53] A. Roy, A.K. Srivastava, B. Singh, T.H. Mahato, D. Shah, A.K. Halve, Microporous Mesoporous Mater. 162 (2012) 207.
[54] T.H. Mahato, B. Singh, A.K. Srivastava, G.K. Prasad, A.R. Srivastava, K. Ganesan, R. Vijayaraghavan, J. Hazard. Mater. 192 (2011) 1890.
[55] R.M. Narske, K.J. Klabunde, S. Fultz, Langmuir 18 (2002) 4819.